SANDIA REPORT

SAND2014
Unlimited Release
Distributed September 2014

In-situ Study of Dynamic Phenomena at Metal Nanosolder Interfaces Using Aberration Corrected Scanning Transmission Electron Microcopy

Ping Lu, Timothy J. Boyle, Michael L. Neville, Daniel T. Yonemoto, Mike Chandross and Blythe Clark

Prepared by
Sandia National Laboratories
Albuquerque, New Mexico 87185 and Livermore, California 94550

Sandia National Laboratories is a multi-program laboratory managed and operated by Sandia Corporation, a wholly owned subsidiary of Lockheed Martin Corporation, for the U.S. Department of Energy's National Nuclear Security Administration under contract DE-AC04-94AL85000.

Issued by Sandia National Laboratories, operated for the United States Department of Energy by Sandia Corporation.

Available to DOE and DOE contractors from
U.S. Department of Energy
Office of Scientific and Technical Information
P.O. Box 62
Oak Ridge, TN 37831

Telephone: (865) 576-8401
Facsimile: (865) 576-5728
E-Mail: reports@adonis.osti.gov
Online ordering: http://www.osti.gov/bridge

Available to the public from
U.S. Department of Commerce
National Technical Information Service
5285 Port Royal Rd.
Springfield, VA 22161

Telephone: (800) 553-6847
Facsimile: (703) 605-6900
E-Mail: orders@ntis.fedworld.gov
Online order: http://www.ntis.gov/help/ordermethods.asp?loc=7-4-0#online

SAND2014-18468
Unlimited Release
September 2014

In-situ Study of Dynamic Phenomena at Metal Nanosolder Interfaces Using Aberration Corrected Scanning Transmission Electron Microcopy

Ping Lu, Timothy J. Boyle, Michael L. Neville, Daniel T. Yonemoto, Mike Chandross and Blythe Clark
Sandia National Laboratories
P.O.Box 5800
Albuquerque, NM 87185

Abstract

Controlling metallic nanoparticle (NP) interactions plays a vital role in the development of new joining techniques (nanosolder) that bond at lower processing temperatures but remain viable at higher temperatures. The primary objective of this project is to develop a fundamental understanding of the actual reaction processes, associated atomic mechanisms, and the resulting microstructure that occur during thermally-driven bond formation concerning metal-metal nano-scale (<50nm) interfaces.

In this LDRD project, we have studied metallic NPs interaction at the elevated temperatures by combining in-situ transmission electron microscopy (TEM) using an aberration-corrected scanning transmission electron microscope (AC-STEM) and atomic-scale modeling such as molecular dynamic (MD) simulations. Various metallic NPs such as Ag, Cu and Au are synthesized by chemical routines. Numerous in-situ experiments were carried out with focus of the research on study of Ag-Cu system. For the first time, using in-situ STEM heating experiments, we directly observed the formation of a 3-dimensional (3-D) epitaxial Cu-Ag core-shell nanoparticle during the thermal interaction of Cu and Ag NPs at elevated temperatures (150 – 300^{o}C). The reaction takes place at temperatures as low as 150^{o}C and was only observed when care was taken to circumvent the effects of electron beam irradiation during STEM imaging. Atomic-scale modeling verified that the Cu-Ag core-shell structure is energetically favored, and indicated that this phenomenon is a nano-scale effect related to the large surface-to-volume ratio of the NPs. The observation potentially can be used for developing new nanosolder technology that uses Ag shell as the “glue” that sticks the particles of Cu together.

The LDRD has led to several journal publications and numerous conference presentations, and a TA. In addition, we have developed new TEM characterization techniques and phase-field modeling tools that can be used for future materials research at Sandia.

Acknowledgements

This work was supported by the Laboratory Directed Research and Development (LDRD) program of Sandia National Laboratories. Sandia National Laboratories is a multi-program laboratory managed and operated by Sandia Corporation, a wholly owned subsidiary of Lockheed Martin Corporation, for the US Department of Energy's National Nuclear Security Administration under contract DE-AC04-94AL85000.

Table of Contents

1. Introduction **6**

2. Synthesis of Nanometals **6**
2.1. Individual nanomaterials 6
2.2. Mixture of nanomaterials 13
2.3. Conclusions 16

3. In-situ STEM study of NP interactions at elevated temperatures **16**
3.1. Experimental 17
3.2. Electron beam effect 17
3.3. Ag-Cu NP interaction 18

4. Atomic-scale modeling **22**
4.1. Modeling details 23
4.2. Modeling results 23
4.3. Model development 27
4.4. Conclusions 31

5. References **32**

6. Journal Publications and Conference presentations/proceedings **33**
6.1. Journal publications 33
6.2. Conference presentations/proceedings 33

1. Introduction

Presumably due to their highly reactive surface properties, the melting temperature of NPs is lower in comparison to bulk materials. This has led to the conjecture that NPs can be used to form nanoalloys at significantly lower temperatures (i.e., nanosolders)[1]. However, the atomistic reaction mechanisms that dominate the NP interface reactions for bond formation at high temperatures remain unknown. The current theories used to describe metal-metal bonding interfaces at high temperatures are based on micron-scale phenomena involving melting, wetting, solid-state diffusion, alloying, phase formation/transformation, and/or combinations of all of these. It is not clear whether these theories can be applied to describe the nano-scale interface interactions. Also, it is not clear as to whether the resulting microstructure (i.e., phase formation/phase transformation) predicted by thermodynamics (i.e., phase diagrams) is still valid at the nano-scale. This is due to the fact that many additional variables exist that influence the thermally induced changes on the nano-scale such as surface chemistry, particle size and morphology, and other unidentified variables.

In order to develop a better, fundamental understanding of the reaction processes and associated atomic mechanisms, and the resulting microstructure of nano-scale metal-metal interfaces at elevated temperatures, in-situ TEM is used in this LDRD project to observe the atomic-scale dynamic behavior of the interface reactions. Additionally, the experimental insight provided by in-situ observations is coupled with atomic-scale, MD modeling, to elucidate the mechanisms of bonding in metal-metal NPs and the influence of physical properties on the reaction mechanism.

Through the project, we have successfully synthesized various metallic NPs such as Ag, Cu, Au, and carried out numerous in-situ experiments. In particular, experimental efforts on Ag-Cu systems have led to discovery of formation of the core-shell Ag/Cu structure at reaction temperatures as low as 150^{o}C. Molecular dynamics (MD) and Monte Carlo (MC) models indicated that the core-shell structure is thermodynamically preferred, and is a nano-scale effect related to the large surface-to-volume ratio of the NPs. These results have also been used to develop a phenomenological (phase-field) model that can used to model the reaction of the nano-scale alloys.

2. Synthesis of nanometals

In this section, we describe the metallic NPs synthesized. The preparative method used is referenced when possible. Powder X-ray diffraction (PXRD) and TEM were used to analyze the synthesized NPs. For the PXRD patterns, a beryllium dome (BeD-XRD) methodology was used to obtain oxide-free patterns when necessary [2].

2.1. Individual nanomaterials.

Several different nanometals were synthesized during the timeframe for the LDRD. The metals were selected based on established solder compositions. Table 1 lists the proposed compositions to be studied. The synthesis of the individual components (i.e., Cu, Ag, Au, Ge, Sn, Pb) as nanometals are discussed below in order.

Table 1. Composition and characteristics of various solders.

metals	composition	Bulk T(melt) ^{o}C
Ag-Cu	28:72	780 (eutectic)
Ag-Au	50:50	1012
Au-Cu	57:43	889
Au-Ge	88:12	361
Au-Sn	80:20	280
Sn-Pb	63:37	183
Sn-Ag	96.5:3.5	221

a. Copper. The synthesis of copper nanoparticles (Cu NP) was undertaken following the mesityl (2,4,6-$Me_3C_6H_2$) preparative route previously established [3]. In general, copper mesityl (Cu(Mes)) was synthesized according to equation 1. For this precursor preparation for nanosolder applications, it is critical that the specific washes and extraction be followed as listed below to isolate 'clean' precursor. If not, a residual organic species remains that complicates the nanomaterials isolated.

CuCl + (Mes)Mg Br → Cu(Mes) + MgBrCl (1)

Premix CuCl (20 g) in THF (100 mL); (b) Add 500 mL of Dioxane:THF (200:300) that has been cooled below room temperature (-35 ^{o}C); (c) let stir for 2 days; (d) turn off stir plate and let sit for at least 1h. (settles out the ppt); (e) filter off precipitate; (f) in vacuo *distillation of volatile component (strip); (g) wash with hexanes; (h) extract with toluene; (i) in vacuo distillation of volatile component (strip). Final product is a pale yellow powder. Should be highly soluble in octylamine.*

Once isolated, the Cu(Mes) is converted to Cu NP following the octylamine (OctN)-hexadecylamine (HDA) process previously developed [3]. The general description is shown in equation 2.

Cu(Mes)/OctN (4.4 g / 10 mL) + HDA (300 ^{o}C) → Cu^{o} + byproducts (2)

(a) transfer HDA to a three neck flask equationuipped with a water-cooled reflux condenser under argon; (b) heat to 300 ^{o}C (wrap in Al-foil); (c) prepare Cu(Mes) in OctN in glovebox – must be fully dissolved; (d) bring out of box and pour directly into hot HDA reaction – excess gas will come off at high temperature; (e) reaction turns deep red; (f) heat for 5 min; (g) pull heat off and allow to cool to room temperature under argon; (h) drop reflux condenser and pump into glovebox; (i) add toluene to dissolve the mixture; (j) pour part into centrifuge tube and fill rest of tube with MeOH (1:5 ratio); (k) centrifuge numerous times.

For this route, Teflon^{TM} sleeves versus grease were used to minimize contamination. Further, all reactions were performed under argon atmosphere to minimize oxide formation. In a glovebox, Cu(Mes) was dissolved in OctN yielding a dark brown-yellow solution. If the sample sits for an extended period of time (30 min) a precipitate will form, so it is recommended that a rapid use of the dissolved precursor be used. Upon addition, which was poured in versus syringe addition to speed up the process, a large gas expulsion follows, so care should be taken. Once reacted, heating of the sample was continued for 5 to 40 min with no major change in size with a red colored solution; however, after 40 min, the sample solution turned to a copper color.

(a) 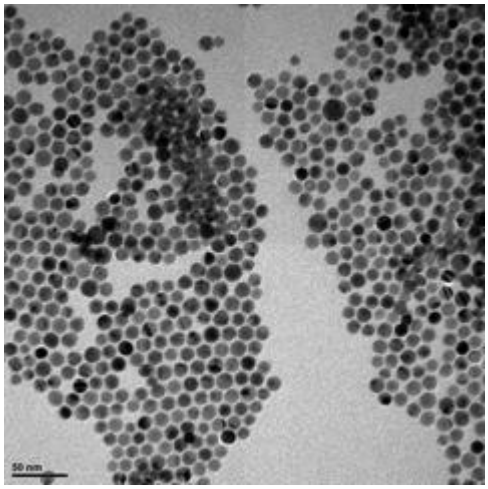 (b) 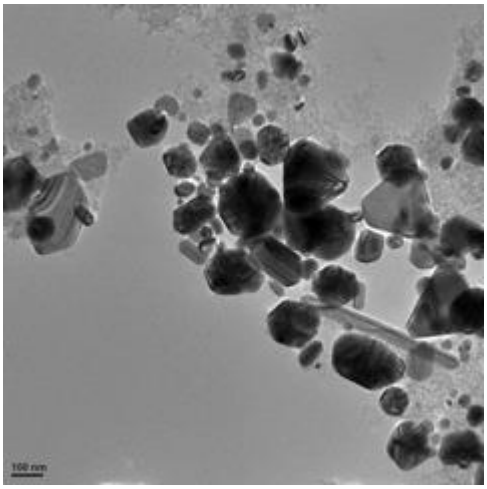

Figure 1. TEM images of Cu NP formed at (a) 5 min and (b) 40 min.

BeD-XRD indicates the samples are Cu^{o}. TEM analysis shows that uniform nanoparticles are formed, especially at (a) 5 min (10-15 nm) and (b) 40+ min (> 100 nm). TEM images of CuNPs synthesized are shown in Figure 1.

b. Silver. Ag NPs were synthesized following literature procedure [4]. In general, the reaction follows equation 3, where a solution of silver acetate, oleylamine, and toluene were added via syringe to toluene at reflux temperatures. After 4 h, the oleylamine reduces Ag(I)to Ag(0) forming a dark brown solution which was allowed to cool and was found to yield nanoparticles around 10 nm in size (see Figure 2). The particles were isolated via centrifugation and washed in a mixture of methanol and hexanes to remove excess oleylamine. TEM was performed and is shown in Figure 2.

AgOAc + oleylamine [tol]→ Ag^{o} + byproducts (3)

(a) transfer hexanes to a three neck flask equationuipped with a water-cooled reflux condenser under argon; (b) heat till reflux begins (c) dissolve AgOAc in oleylamine and add to syringe; (d)add AgOAc solution to the hexanes via syrringe; (e) reaction turns yellow; (f) heat for 4 hours; (g) pull heat off and allow to cool to room temperature under argon; (h) add methanol to crash AgNP out of solution and centrifuge; (i) wash with mixture of hexanes and methanol (1:10) and centrifuge; (j) decant the liquid leaving the AgNP; (k) repeat (i) & (j) three times to yield clean AgNP.

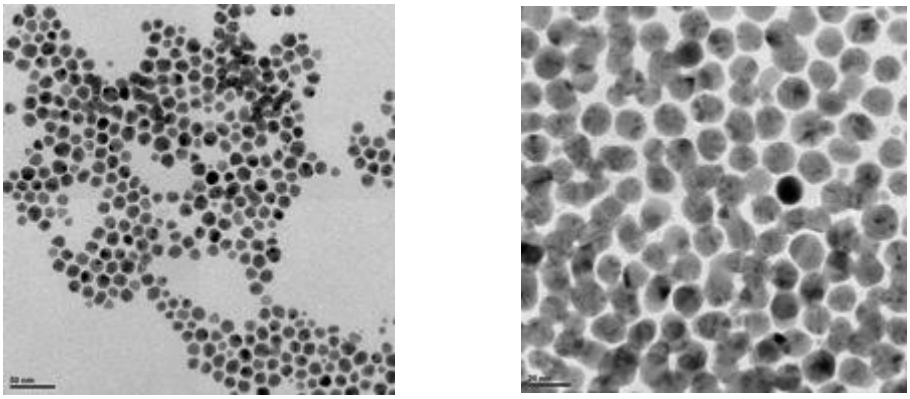

Figure 2. Characteristic TEM images of AgNP formed.

c. Gold. The synthesis of gold nanoparticles was performed via the reaction of tetrachloroauric acid and oleylamine in a solvent following a previously disseminated route [4]. The reaction is the reduction of auric acid by oleyleamine at elevated temperatures (see equation 4). TEM analysis shows the particles with a uniform size distribution, and particles size less than 20 nm in diameter, as shown in Figure 3:

$$\mathbf{HAuCl_4 + oleylamine \rightarrow Au^0 + byproducts} \qquad \mathbf{(4)}$$

(a) dissolve AuCl in oleylamine (1g:25mL); (b) transfer to a three neck flask equationuipped with a water-cooled reflux condenser under argon; (c) heat; (d) in a separate flask cool ethanol via an ice bath; (e) once solvent has reached temperature, inject Au oleylamine mixture; (f) after 30 min reaction will turn to a red/purple color (g) pull heat off and quench with EtOH under argon; (h) vacuum distill off excess solvent; (i) centrifuge with MeOH (1:5 ratio) 3 times.

(a) (b)

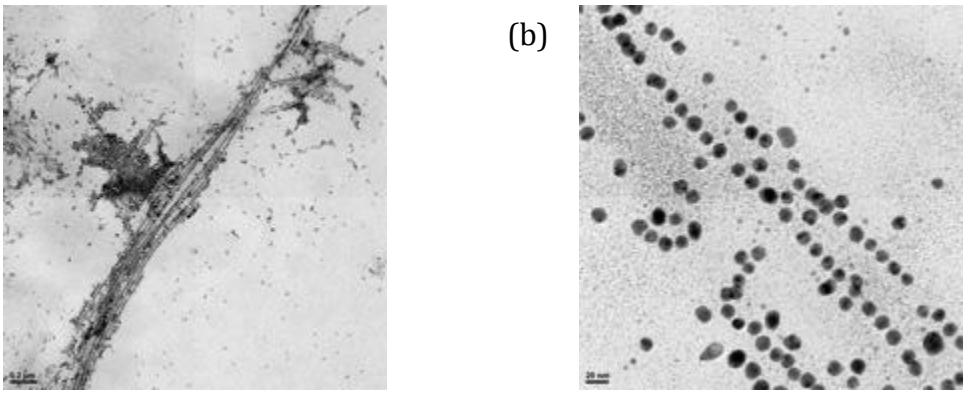

Figure 3. Characteristic TEM images of Au NP.

d. Germanium. Ge NP were synthesized following literature procedure [5, 6]. Initially, germanium (II) bis(trimethylsilyl amide) ($Ge(NR_2)$ was isolated from the reaction shown in equation 5.

$$GeCl_2(dioxane) + 2\,K(NR_2) \rightarrow Ge(NR_2)_2 + 2\,KCl \quad (5)$$

$$Ge(NR_2)_2 + oleylamine + octadecene \rightarrow Ge^0 + byproducts \quad (6)$$

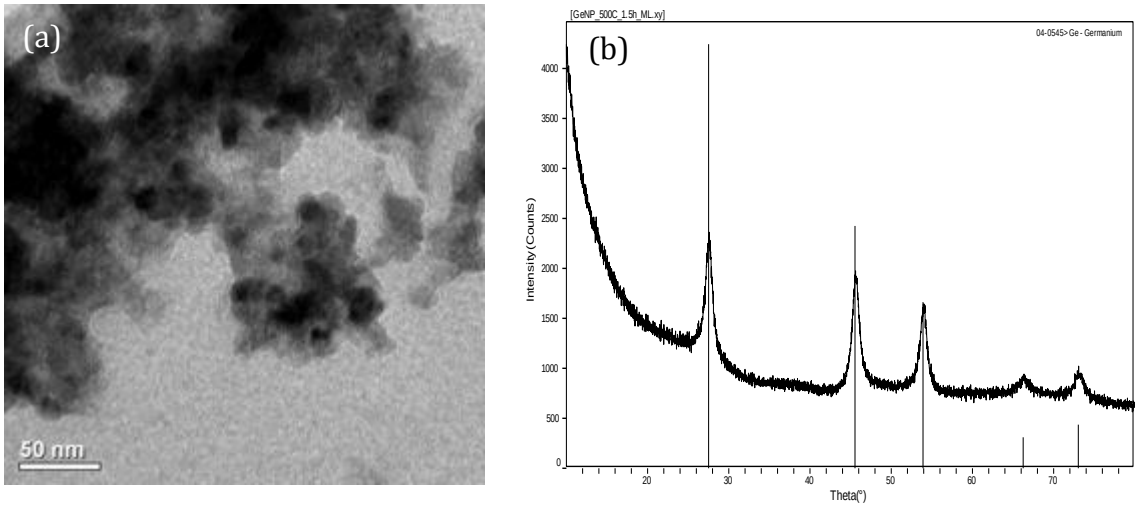

Figure 4. (a) TEM image and (b) PXRD of Ge NP.

Once synthesized, the resulting orange oil was dissolved in oleylamine and then rapidly injected into octadecene heated to 300 ^oC (equation 6). The particles were isolated by washing with chloroform and iso-propanol (50:50) solution. These particles were not distinct (see Figure 4a) but rough and irregular. PXRD pattern (Figure 4b) indicates that the material was phase pure Ge^o.

e. Tin. A similar pathway as for Ge was used for the initial Sn^o efforts. For the $Sn(NR_2)_2$ precursor, the powder isolated was found to be tin oxide (Figure 5).

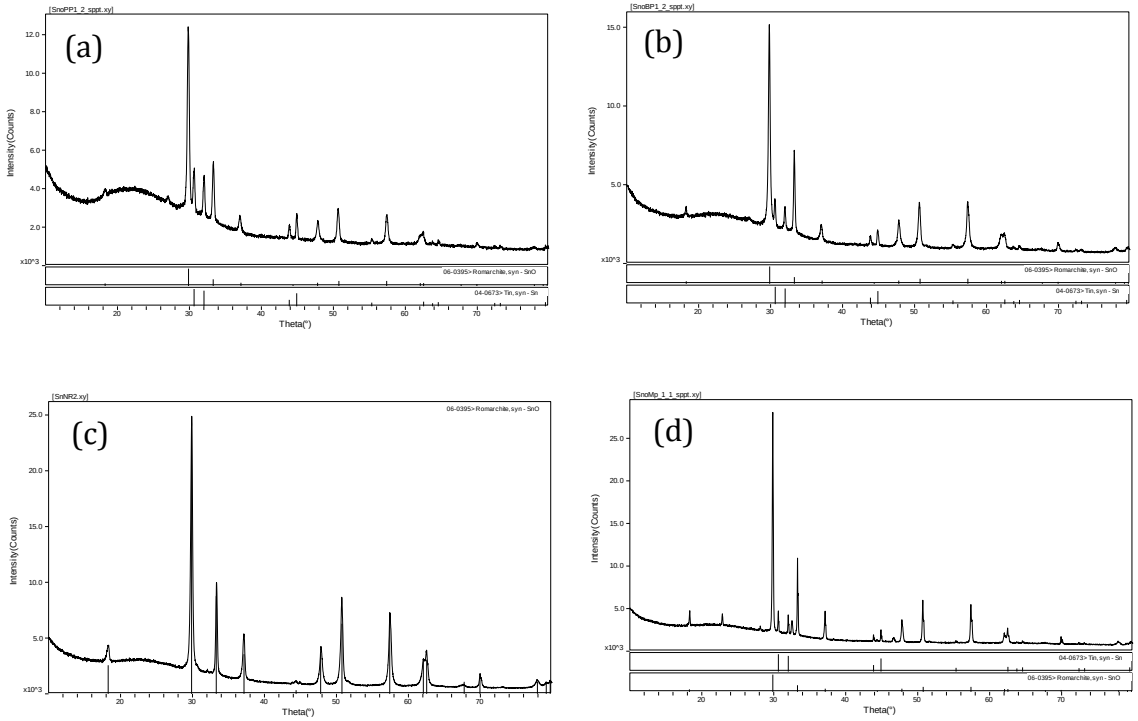

Figure 5. PXRD of NPs from (a) $Sn(NR_2)_2$, (b) $Sn(oMP)_2$, (c) $Sn(oPP)_2$, and (d) $Sn(oBP)_2$.

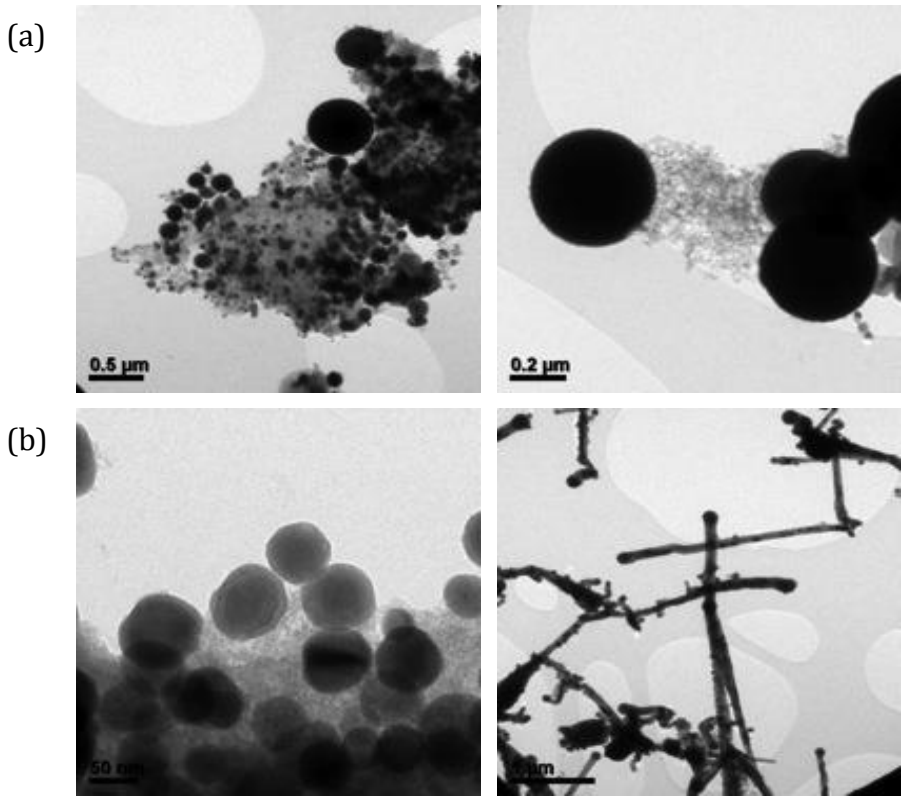

Figure 6. TEM images of NPs generated from (a) $Sn(oMP)_2$ and (b) $Sn(oBP)_2$.

Switching to alkoxide precursors worked to alter the morphology of the Ge NP and was attempted in this instance. For the ortho substituted phenoxide (methyl (*o*MP); propyl (*o*PP); butyl (*o*BP)) derivatives, under similar conditions, a mixture of oxide and metal were isolated. The PXRD patterns are shown in Figure 5, for *o*MP and *o*BP, respectively. TEM images were collected on these samples and are shown in Figures 6a, and 6b, respectively. The obvious large particle spheres are most likely the metal with the smaller shaped particles being the oxide. These cannot be considered nano and were therefore not pursued. Interestingly, wires were formed by the *o*BP species but could not be generated consistently. The inability to isolate the oxide free species prevented additional work with these materials.

f. Lead. The same approach was used for the production of Pb^o NP. The amide was synthesized according to equation 7. Once isolated this yellow powder was dissolved in oleylamine and injected into octadecene at high temperature. The resultant products were found by PXRD to be Pb^o (Figure 7a) but the TEM images (Figure 7b) revealed poorly defined nanomaterials. These were not pursued further.

$$\mathbf{PbCl_2 + 2\,KNR_2 \rightarrow Pb(NR_2)_2 + 2KCl} \quad \mathbf{(7)}$$

(a)

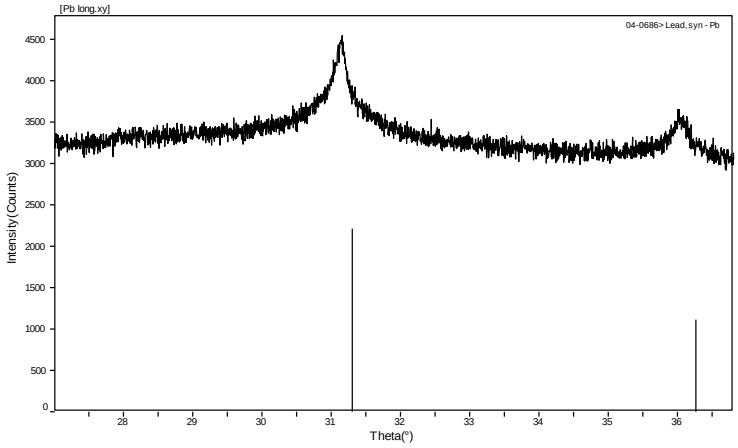

(b)

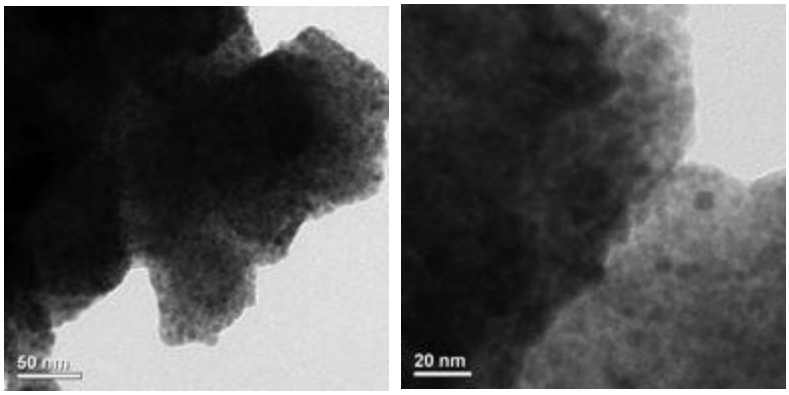

Figure 7. (a) PXRD and (b) TEM images of the synthesized of Pb^o.

2.1. Mixture of nanomaterials.

Using the above nanomaterials mixtures of the nanometals were synthesized for analysis. The mixtures were made by combining dissolved samples. In general, 20 mg of each dried product was dissolved in toluene and stoichiometric ally mixed as follows in equations 8-10 and TEM images collected on the resultant mixtures.

$$Cu^{o} + Au^{o} \rightarrow \quad (8)$$
$$Ag^{o} + Au^{o} \rightarrow \quad (9)$$
$$Ag^{o} + Cu^{o} \rightarrow \quad (10)$$

For equation 8, the Au/Cu sample (Au/Cu #1) was prepared in an argon glovebox with an approximate 1:1 stoichiometric mixture of the individual nanoparticles in toluene. Upon mixing, the resulting solution took on a predominately purple color. The resulting solution was dropped onto a TEM grid and allowed to dry. The images obtained are shown in Figure 8.

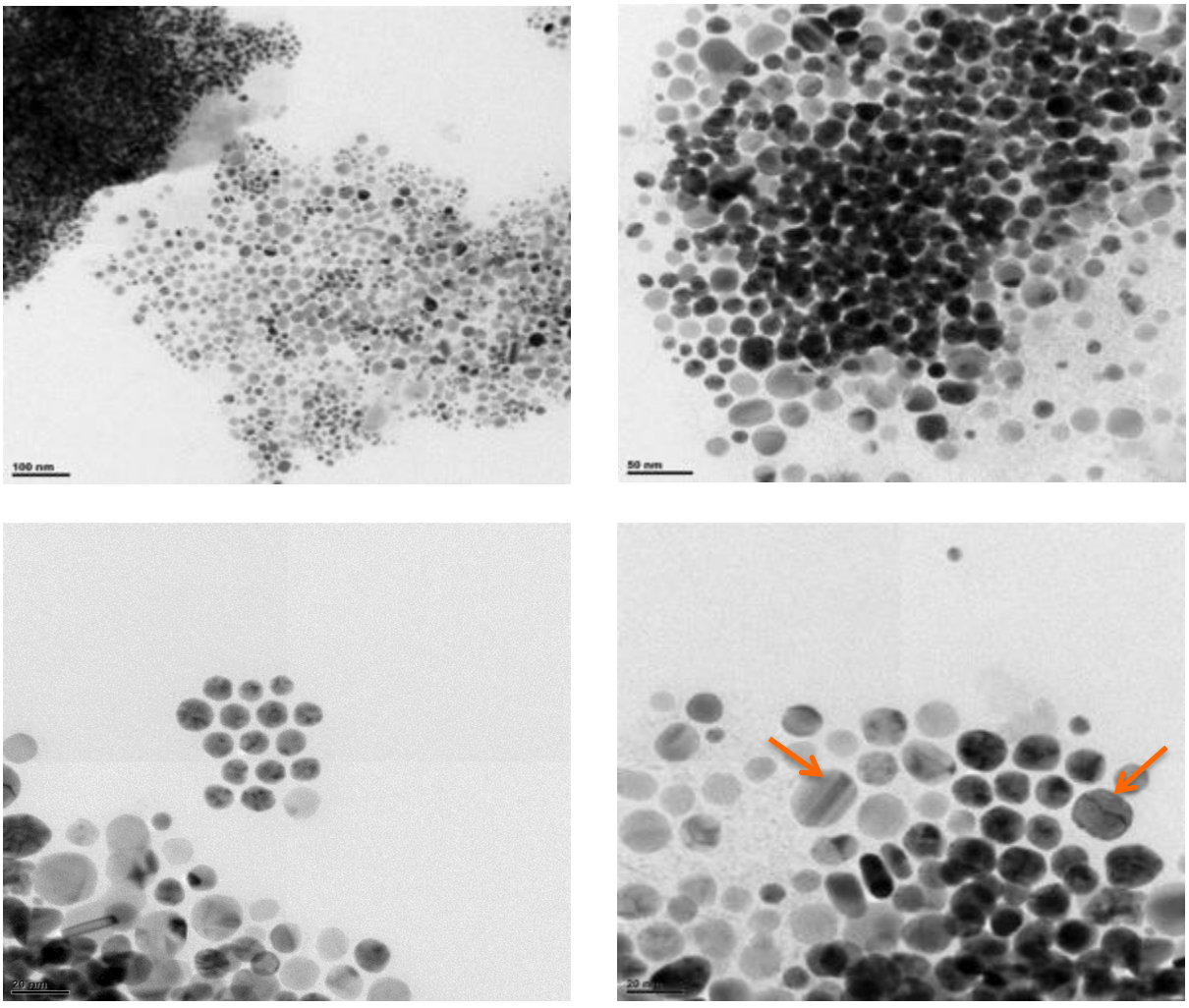

Figure 8. TEM images for Au/Cu NP mixture. Orange arrows highlights what appears to be mixed NPs.

A contrast can be seen on numerous particles indicating a successful interaction between the two metals, however EDS is required to confirm these results. The observed mixed particles (see arrow) appear different from the encapsulation noted for the Cu/Au system. Additional studies on the growth mechanism is needed.

The next sample (Figure 9 – Au/Cu #2) also consisted of mixtures of Au and Cu nanoparticles. The same di-phasic nanoparticle was not observed. Based on size, there only appears to be one type of nanoparticle present in the sample; however, this conclusion cannot be supported without more data.

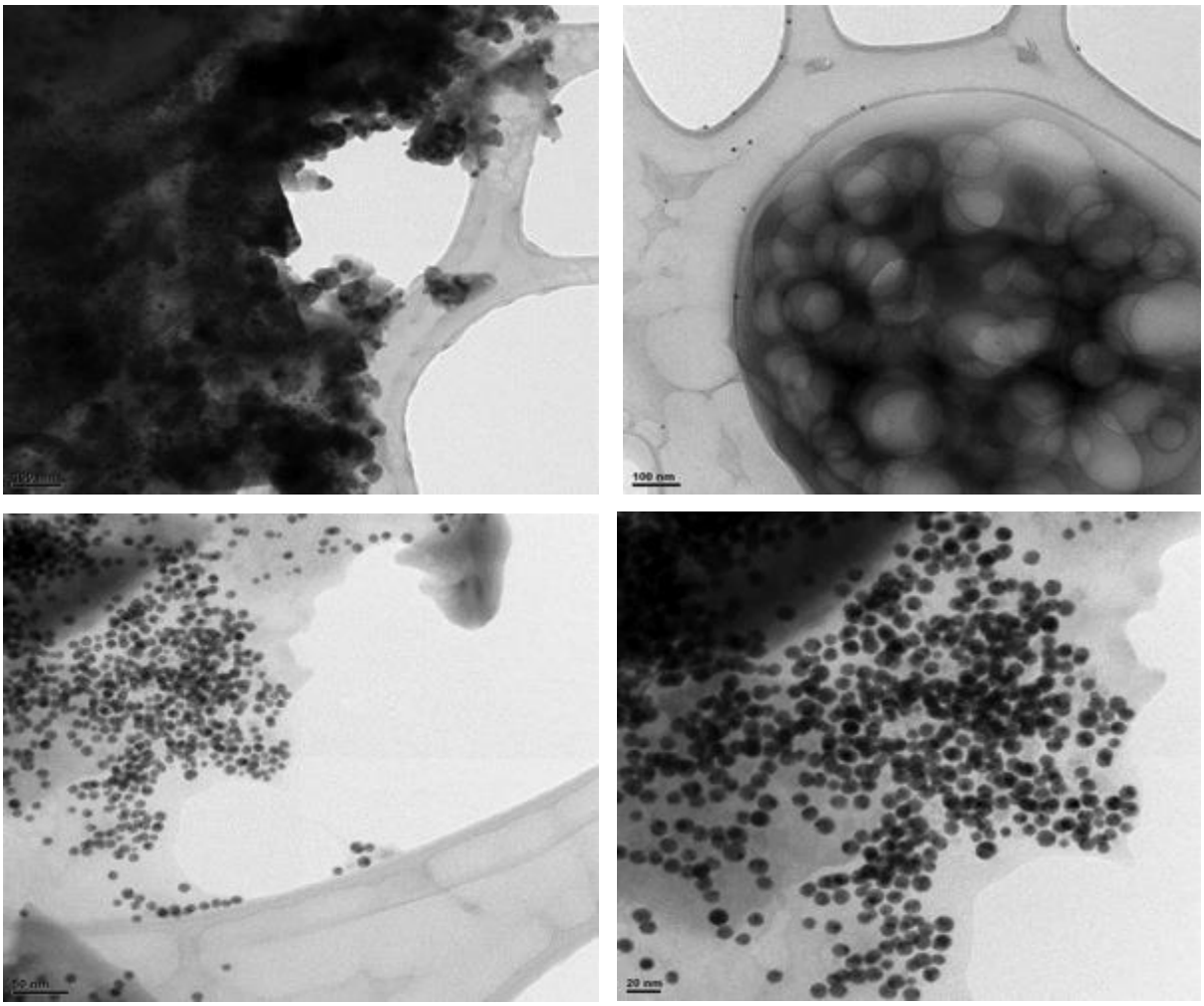

Figure 9. TEM image of the Au/Cu mixture #2.

Additional mixtures were undertaken following equation 9. A mixture of Ag^0/Au^0 nanoparticles was generated as well with the expectation that these would form a single solid solution of Ag-Au. TEM images of the materials isolated are shown in Figure 10. Again, based on size, there appears to be two types of nanoparticles in the sample that appear to comingling (5 and 20 nm).

However, due to the occasional resizing of the silver upon re-dissolution and the lack of EDS, no definitive conclusions can be made about the composition.

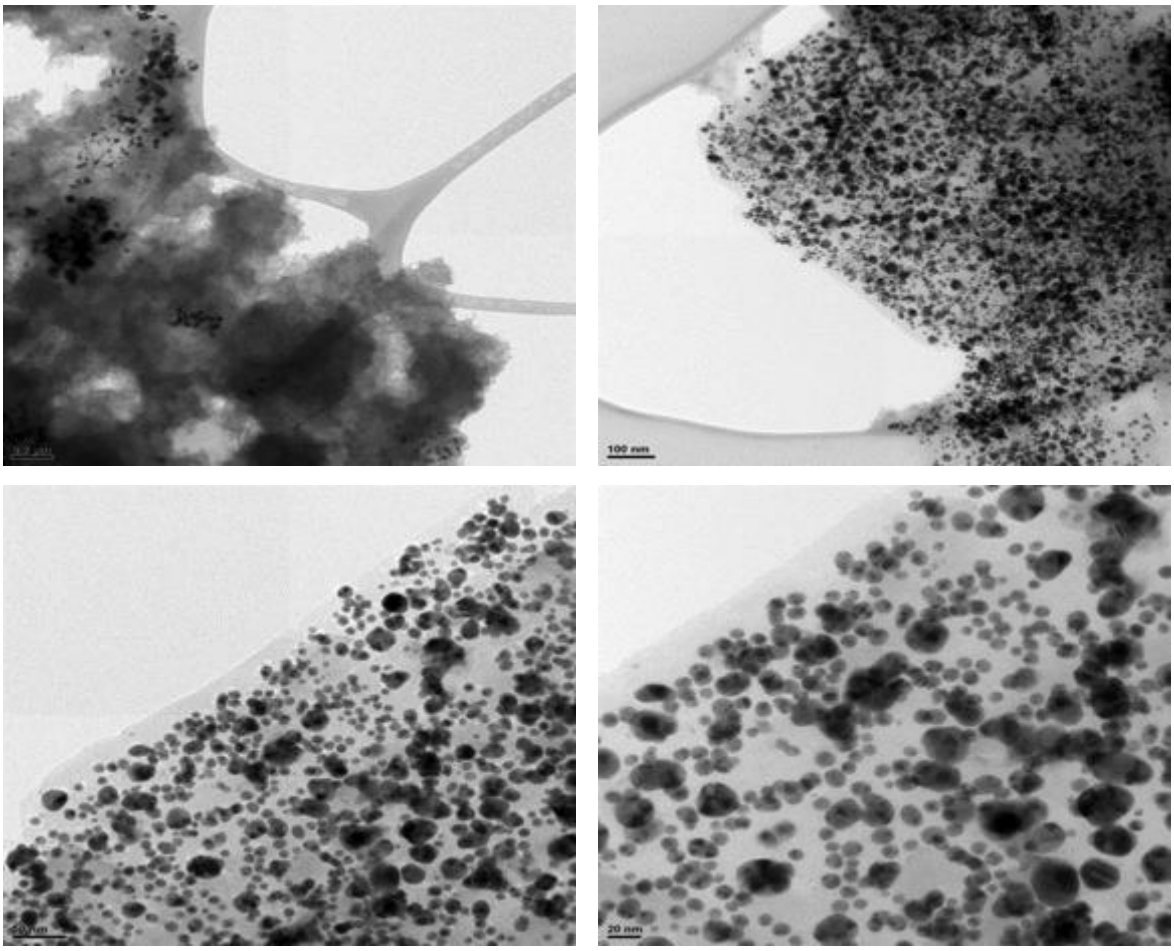

Figure 10. TEM images of Ag/Au mixture.

Finally, a Ag/Cu NP mixture (equation 10) was generated in a similar phase as above. The sample is shown in Figure 11. We found that after drying the silver, when re-dissolved, the particles can grow in size from sub 20 to 200 nm. There are smaller particles that would be consistent with the Cu NP.

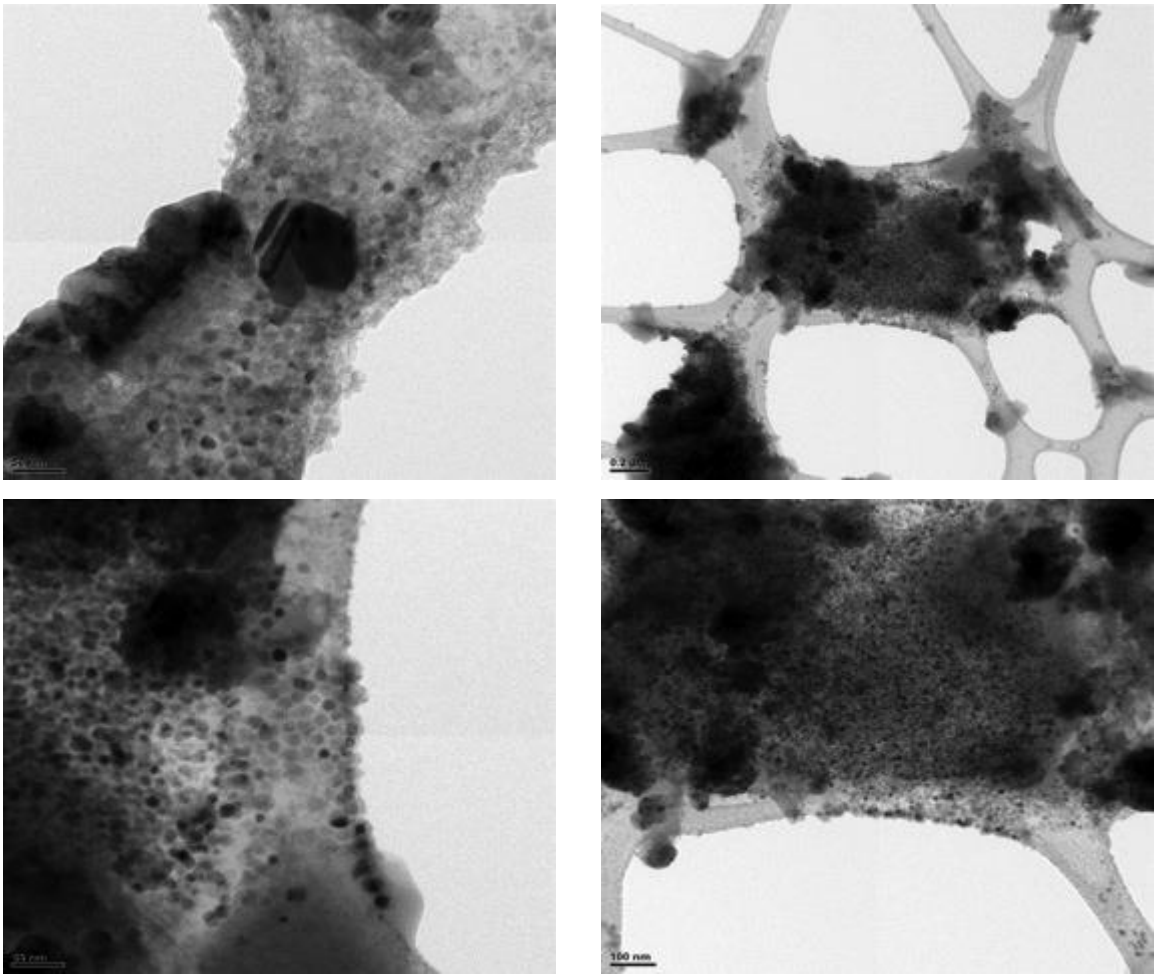

Figure 11. TEM images of Ag/Cu mixture.

2.3. Conclusions

The various metallic NPs were successfully synthesized and isolated, and these NPs can be used as starting materials for in-situ TEM study. In particular, the Cu, Ag NPs were successfully isolated, and these NPs are extremely pure and highly uniform in size. The NPs of different metals were also mixed in an effective 1:1 stoichiometry and analyzed by TEM. While EDS is necessary for each of these samples, it does appear several have interesting interactions at room temperature.

3. In-situ STEM study of NP interaction at elevated temperatures

In this session, we describe the in-situ STEM observations of NP interactions at elevated temperatures. The in-situ STEM study was primarily focused on the Ag-Cu NP system due to availability of the high purity, and uniform-sized Ag, and Cu NPs as well as relevance of the system for nanosolder applications [1, 7-10]. Various experiments (more than 50) were carried out during the LDRD.

3.1. Experimental

The Cu and Ag NPs used for the in-situ STEM had an average diameter of ~12 nm and 6 nm, respectively. The TEM specimen was made by pre-mixing the NPs in toluene and placing a drop of the mixed solution on a thin carbon film (<5 nm) supported by the TEM grid. By adjusting the solution concentration, Cu and Ag NPs could be assembled on the carbon film such that a monolayer of NPs was formed. Figure 12 shows a typical TEM image of the Cu-Ag NPs prior to heating. Based on this image, it is apparent that the larger Cu and smaller Ag NPs are well mixed, with the smaller Ag NPs present in between and in contact with Cu NPs. This intimacy is critical for initiating the Cu-Ag reaction, since a competitive low temperature Ag-Ag reaction also takes place during the heating.

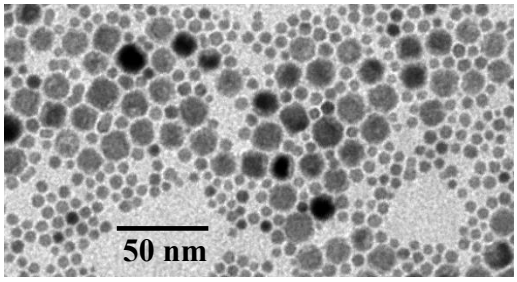

Figure12. TEM image showing a typical monolayer of Cu (~12nm) and Ag(~6nm) NPs assembled on a carbon film prior to in situ heating.

Generally, in-situ electron microscopy is performed in a TEM mode, which offers a real-time observation capability. However, during this study, it was determined that electron beam irradiation of the sample during TEM/STEM imaging severely impacted the Cu-Ag interaction process, preventing real-time observations from being made. The electron beam effect is described in section 3.2.

In-situ STEM heating experiments were carried out using the Protochips Aduro™ in-situ heating stage, which is capable of extremely fast heating and cooling rates (1000 ^{o}C/s) [11]. A FEI Titan™ G2 80-200 STEM with a Cs probe corrector and ChemiSTEM™ technology (X-FEG™ and SuperX™ energy-dispersive X-ray spectroscopy (EDS) with four windowless silicon drift detectors), operated at 200 kV, was used in this study. The microscope was normally operated in the scanning mode and a high-angle annular dark-field (HAADF) detector was used to record STEM HAADF images, which are sensitive to atomic-number (Z) [12].

3.2. Electron beam effect

Electron beam exposure to NPs can lead to several effects. For example, exposure to Ag NPs for as little as 60 seconds renders the NPs inactive. Figure 13 shows the HAADF image showing Ag NPs after in-situ heating at 160^{o}C for 5 min with and without the pre-electron exposure. The Ag NPs had a size of ~ 6nm before the heating. The Ag NPs on the left side of the image in Figure 13 were pre-exposed with the electron beam under a normal STEM mode for about 1 min, and the Ag NPs on the right side of the image were without prior electron exposure. The comparison

image shows that electron beam exposure makes the Ag NPs less active during the heating experiments.

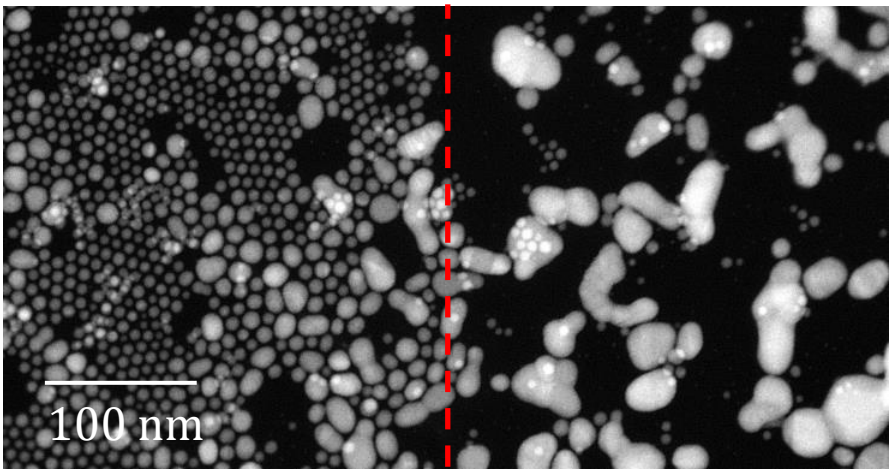

Figure 13. HAADF image showing the effect of the electron beam exposure on the NPs reactivity.

The change in reactivity is likely due to the formation of a carbon shell around the NPs, similar to that found on Au NPs under electron irradiation by Sutter et al. (although this was observed at a higher temperature) [13].

Oxidation of NPs is another possible beam induced effect. Figure 14 shows HAADF images of Ag-Cu NPs formed initially by in-situ reaction (a) and after electron beam exposure for 10 minutes (b) and 20 minutes (c), and EDS elemental maps (d, e, f) obtained for the particles in (c). The Cu becomes gradually oxidized under electron beam exposure, and the oxidations forms a CuOx shell around the Cu NPs as clearly visible in EDS maps in Figure 14.

3.3. Ag-Cu NP reaction

As a result of electron beam effect, the in-situ heating experiments was performed with the electron beam off or with the electron beam on only for the times (typically, less than 30 sec), necessary to obtain the STEM images.

After carefully avoiding irradiation effects from energetic electrons, distinct Ag (~6 nm) and Cu (~12 nm) NPs that are in contact were first found to react by the Ag wetting Cu along the {111} surfaces. Over time this led to a 3-D, cube-on-cube epitaxial Cu-core and Ag-shell structure. This interaction takes place at temperatures as low as 150 ^{o}C and up to 300 ^{o}C. Over 300 ^{o}C, the volatility of the Ag NPs becomes an issue, with most of the Ag NPs evaporating.

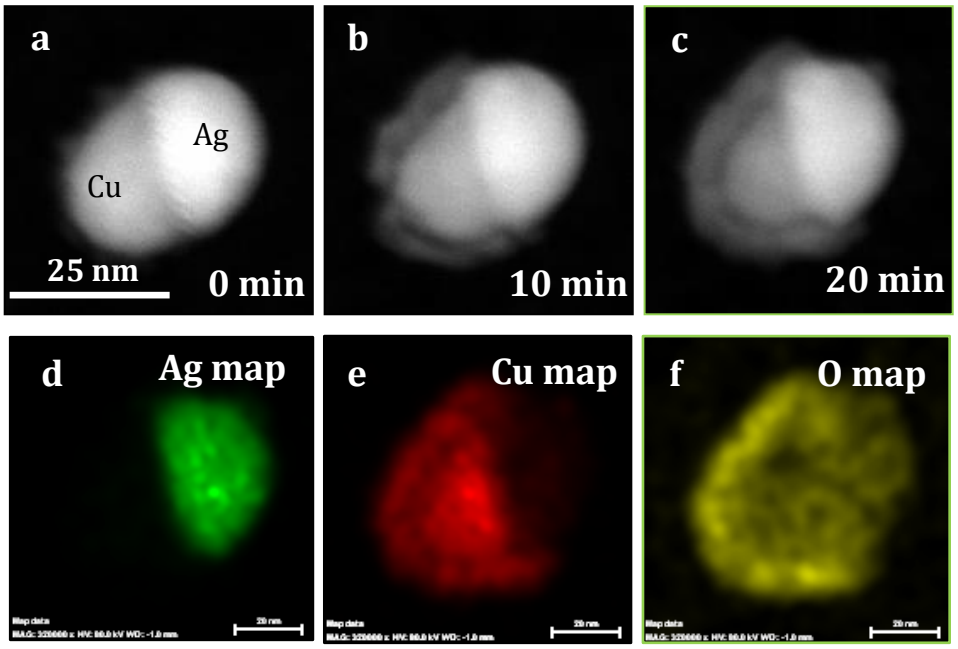

Figure 14. HAADF images of the Cu/Ag NP formed by Cu-Ag NPs interaction (a), and the same particles after exposure to electron beam for about 10 minutes (b) and 20 minutes (c). EDS elemental maps of Ag (d), Cu (e) and O (f), obtained from the particle (c).

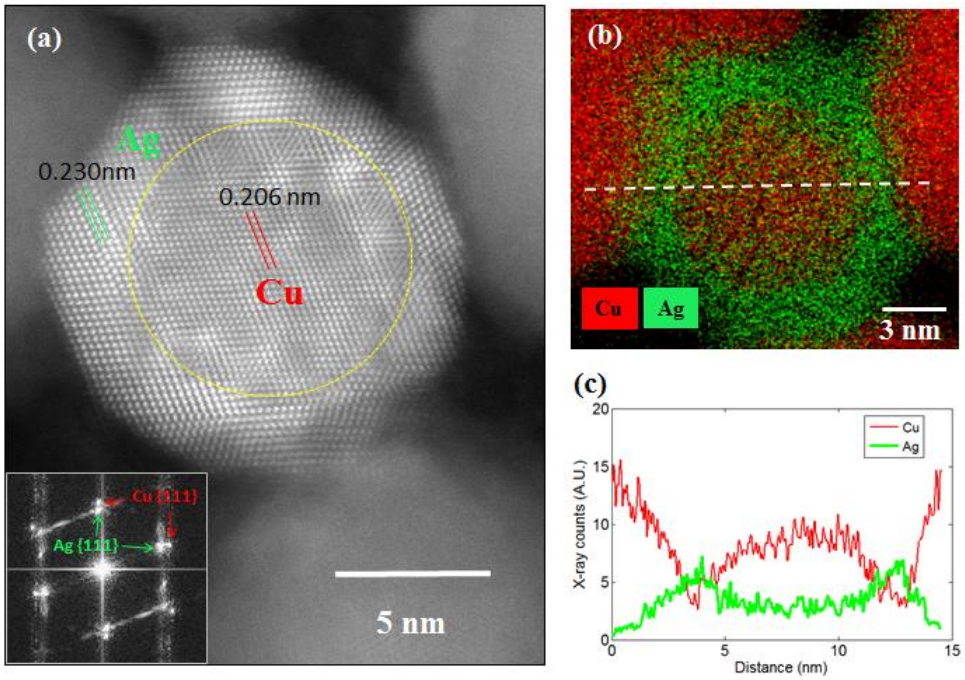

Figure 15. (a) High-resolution HAADF image of a Cu-Ag core-shell particle formed at 150 ^{o}C, along with an inset showing a FFT pattern from the particles; (b) EDS element map of Cu and Ag obtained from the core-shell particle and (c) the EDS line-profile of Cu and Ag along the dashed line marked in (b).

Figure 15a shows a high-resolution HAADF image of the core-shell structure formed at 150 ^{o}C with a Cu-core of ~9 nm in diameter and Ag-shell thickness of ~3 nm. The core-shell structure can be clearly determined by Z-contrast of the HAADF imaging as well as a lattice spacing measurement by using the FFT image from the particle shown in the inset. The measured {111} lattice spacings of the Cu-core and Ag-shell are 0.206 nm and 0.230 nm, respectively; whereas, the {111} lattice spacings for bulk Cu and Ag are 0.209 nm and 0.236 nm, or about 1.4% and 2.5% larger than those measured from the core-shell particles. The moiré fringes in Figure 15a show overlap between Ag and Cu atoms in the electron beam direction, indicating the Ag is present on the top and/or bottom surface(s) of the Cu core. The Ag shell forms predominately in a cube-on-cube orientation relationship with the Cu core, i.e. the cubic planes are parallel. Stacking faults and twin-boundaries are present in parts of the Ag shell.

The Cu-Ag core-shell structure was further confirmed by an EDS element map, shown in Figure 15b, and in an EDS line-profile across the particles shown in Figure 15c. It should be noted that the EDS map in Figure 15b reveals a particle with a somewhat different shape than that observed in Figure 15a. This is due to the continuously changing Ag-shell that evolves when exposed to electron beam irradiation during EDS acquisition. Both the EDS element map and line-profile, however, clearly indicate the particle has the Cu-Ag core-shell structure.

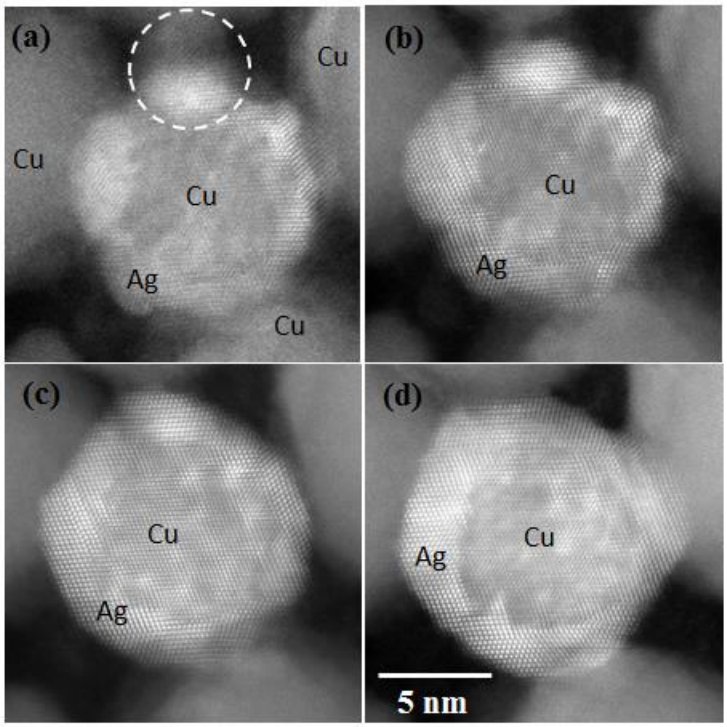

Figure 16. HAADF images showing the formation process of a Cu-Ag core-shell particle: (a) a partially formed core-shell particle at 150 ^{o}C and images of the same particle after additional heating at 150 ^{o}C for (b) 3, (c) 6, and (c) 13 min.

A series of HAADF images showing the process of the core-shell particle formation during heating is shown in Figure 16. Figure 16a shows a particle with the core-shell structure that has partially formed. It can be observed that a Ag NP (marked by a dashed circle near the top of the image) has started to become part of the Ag shell but has not completely merged. Continuous heating at 150 ^{o}C for ~3 min leads to a particle with a more fully formed core-shell structure, as shown in Figure 16b. Further heating for an additional 3 min gives rise to the final core-shell structure (Figure 16c). The moiré fringes at the Cu core become better developed over time as can be clearly observed from Figure 16a to Figure 16c, indicating that the Ag has gradually enveloped the Cu-core. The Cu-Ag core-shell structure (Figure 16c) appears to be stable so long as it stays isolated and no new reactions are initiated with neighboring particles. Figure 16d shows the particle after an additional 7 min of in-situ heating at 150 ^{o}C. As can be observed, with continued heating the Ag shell began new interactions with the Cu particles to its right and in the lower-right corner. In between collection of each image, the electron beam was kept off to reduce possible electron beam irradiation effects.

The initial Cu-Ag NP reaction involves the Ag wetting on Cu surfaces, forming predominately Ag{111}/Cu{111} interfaces. Figure 17 shows the initial structure of the reaction between Cu and Ag NPs at 200 ^{o}C. The Ag, which has a brighter contrast in the HAADF image, has wet several Cu NPs in multiple locations as marked by arrows in the image. The inset image in Figure 17 shows that the Ag{111}/Cu{111} epitaxial interface is sharp and forms between Ag surface layers, as thin as 2-3 {111} monolayers, and the Cu. Although it is difficult to determine the exact chemical composition of the thin surface Ag layer directly, the lattice spacing measured from the brighter Ag layer is about 0.236 nm, consistent with pure Ag.

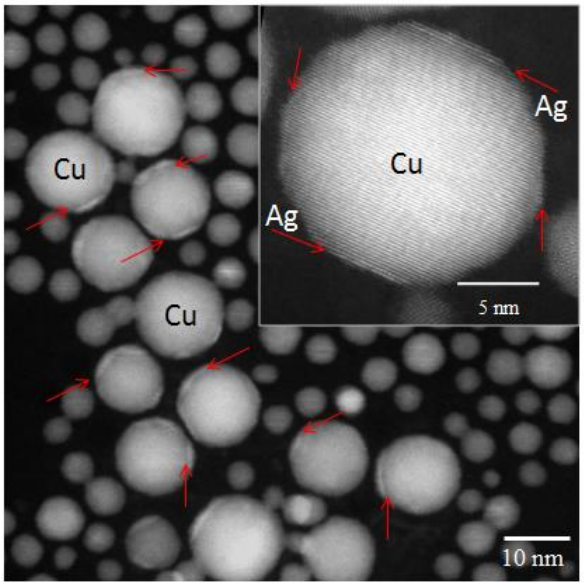

Figure 17. A HAADF image showing the initial reaction between Cu and Ag NPs at 200 ^{o}C. The arrows show the interfaces where Ag wets the Cu NPs. The inset shows a magnified image showing that Ag as thin as 2-3 {111} Ag monolayers has formed at the Ag{111}/Cu{111} interface.

Because they are easily oxidized, the Cu NPs used for some of these experiments had a thin Cu_2O layer on their surfaces when they reacted with the Ag NPs. Interestingly, it was determined that the presence of a thin Cu oxide layer did not affect the overall reaction that forms the Cu-Ag core-shell structure. Figure 18 shows a series of HAADF images taken from the same area after heating at different temperatures and times. A darker layer of ~2 nm in thickness is present on most of the Cu NPs in Figure 18a. This layer, identified as Cu_2O by high-resolution HAADF imaging, resulted from Cu oxidation in air and is apparently still present after *in situ* heating at 150 ^oC for about 2 min. Figure 18b, taken after heating at 180 ^oC for 30 min, shows that the oxide layers are partially removed from some Cu NPs, and that several Ag-Cu NPs with the core-shell structure have formed during the heating. Finally, in Figure 18c, taken after additional heating at 200 ^oC for about 10 min, there are at least six NPs with the Cu-Ag core-shell structure. While the presence of a thin Cu_2O layer on Cu NPs may have delayed the reaction between the two metals, it does not prevent the final formation of the core-shell structure.

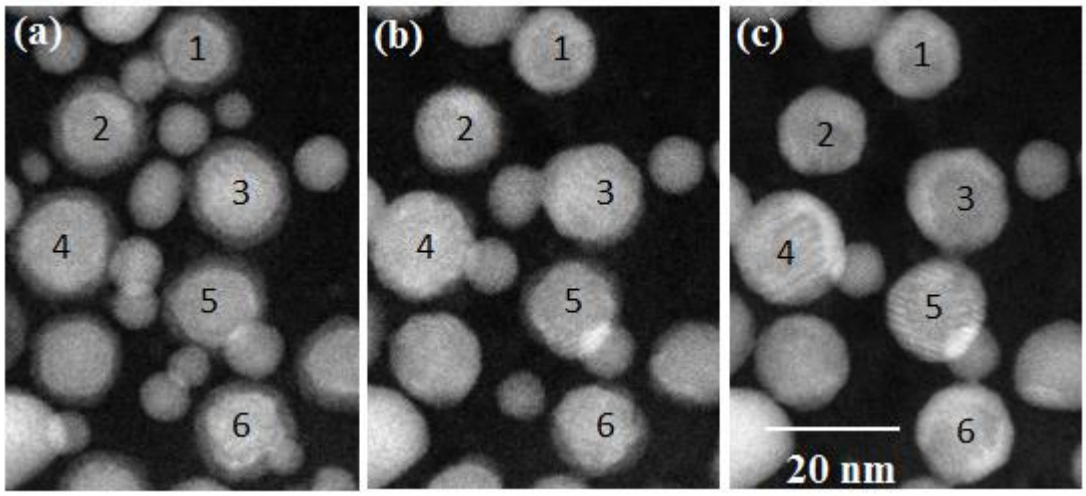

Figure 18. HAADF images taken after sequential heating segments: (a) 150 ^oC for 2 min (the darker layer is Cu_2O); (b) 180 ^oC for 30 min and (c) 200 ^oC for 10 min (The Cu-Ag core-shell NPs are marked by 1 - 6).

4. Atomic-scale modeling

In this work, the formation of the core-shell structure from a surface energy perspective was undertaken, with examples elucidating the optimal sizes from both Monte Carlo (MC) and molecular dynamics (MD) simulations. The results of these simulations were fitted to simple forms, which were then used to develop a phenomenological model of the energetics of the core-shell structure. In particular, the energy gained upon formation of this structure was examined as a function of the radii of the two initial nanoparticles to guide synthesis efforts.

4.1. Simulation Details

MD simulations were performed with the LAMMPS code using the embedded atom method (EAM) with a Cu-Ag alloy potential developed by Williams, *et al*. [15]. A timestep of 1 fs with a velocity Verlet algorithm was used for the integration with the temperature controlled by a Langevin thermostat. The results obtained from the experimental aspect of this project [14] indicated that the core-shell structure forms at temperatures as low as 423 K over a time scale of minutes. Modeling this process is far beyond the timescales accessible by MD simulations. It is therefore appropriate to raise the temperature of the simulations in order to increase the diffusive motion of the atoms. The phase diagram of AgCu binary alloys is a simple eutectic, with a eutectic temperature of 1053 K; however, the EAM potential used underestimates this temperature as 935 K [15]. For the MD runs, the goal was to increase the temperature as high as is feasible for increased diffusion, while remaining below the eutectic line. Initial simulations at 723 K indicated that the initial formation of the core-shell structure occurred rapidly but progression to a final equilibrium structure was excessively slow. Therefore the results of the core-shell formation that were run are presented at a temperature of 923 K.

MC simulations were performed with an in-house code [16], in which Metropolis moves were accomplished by particle swaps with an additional random translation of up to 0.2 Å in any direction. The temperature of the MC simulations was set at 800 K, which is somewhat lower than what was used in the MD models. These results are compared to those at higher temperatures, and while no qualitative difference at 923 K (i.e., the temperature of the MD simulations) could be elucidated, runs at 1200 K (far above the eutectic temperature) showed complete melting and mixing of the system. Therefore, the 800 K MC results represent the structures found at temperatures below the eutectic, without the necessity of using as high a temperature as is feasible, as is the case for the MD simulations. The results are qualitatively similar as there are no structural changes or phase transformations in this region of the phase diagram. Runs were continued until visual inspection indicated an obvious trajectory towards a final state, although these simulations could not establish an equilibrium structure.

4.2. Simulation Results

Simulations began with either Ag or Cu (see Figure 19) nanoparticles of specified radii that were cut from a large block of FCC material. While it is not expected that experimentally synthesized nanoparticles are spherical, particularly at small sizes, this starting geometry is reasonable for accessing the effects of different surface energies on a final state, and allows us the flexibility to develop a phenomenological model. It is expected, however, that final state geometries will more accurately represent experimental systems (see, for example, the faceting in Figure. 19c). Because of the large barriers for diffusion reported for Ag along Cu surfaces [17], these simulations only show the general trend of the shell formation. Select snapshots of the simulation results over time are shown in Figure 19. Runs for the MD calculations began with a 5 nm particle of Ag and Cu that were touching at a single interface along the (010) face (Figure. 1a in contact, after energy minimization, prior to dynamics). Figure. 19b reveals the same particles after 35 ns of runtime (T = 923 K) and clearly shows that the Ag atoms diffuse along the outer surface of the Cu particle (preferring step edges on the {111} plane) and not through the interior. This is in agreement with literature calculations from Baletto and co-workers [17],

which reported the lowest energy barrier for Ag atom on a Cu surface exists for jumps along {111} facets. This is also in agreement with our experimental results [14].

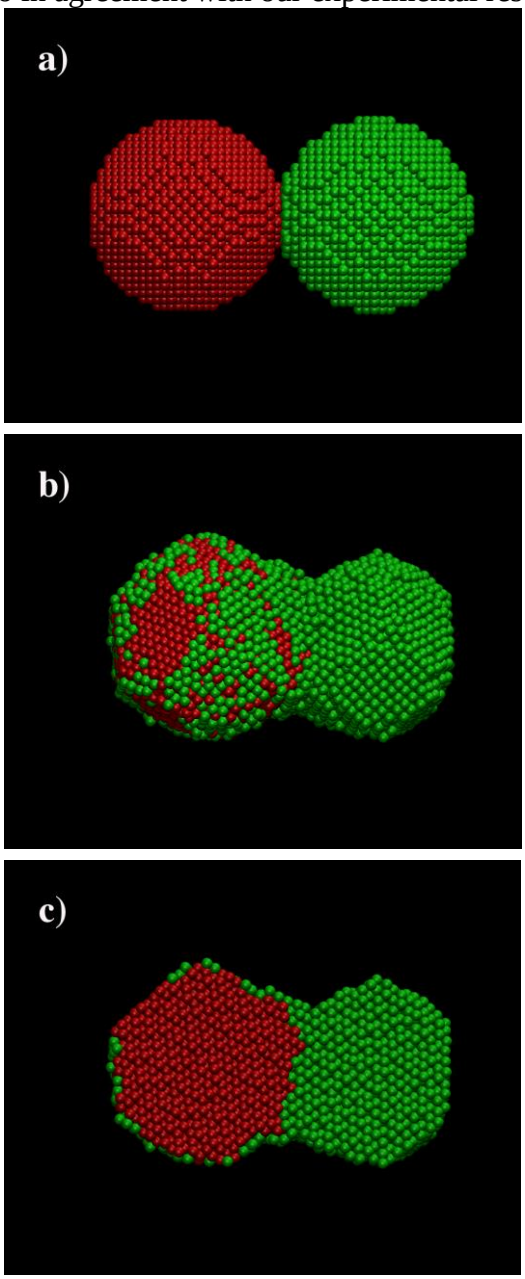

Figure 19. Snapshots from the MD simulation at (a) 0 ns (b) 35 ns and (c) 35 ns in cross-section. Silver atoms are shown as green and copper atoms as red.

The slow formation of the Ag shell essentially moves the time scale out of the range of MD simulations, even at the elevated temperatures employed. Therefore, MC simulations were investigated to arrive at a better picture of the ending state. As described above, the MC code used here performs random particle swaps (in this case, attempting to exchange Cu for Ag atoms

at each MC step) with a small (<0.2 Å), random translation. Therefore, the process of changing the initial shape of the structure (e.g., from two spherical particles as in the MD simulations to a single spherical core-shell structure) would be exceedingly slow. Instead, a spherical structure, in which one side was composed entirely of Cu atoms and the other entirely of Ag atoms, was used and is hereafter referred to as a janus-NP. The results from the MC simulations are shown in Figure 20. The initial janus-NP shown (Figure 20a) consists of a particle with a radius of 5 nm that is divided spatially which results in an unequal number of Ag and Cu atoms.

After 400 million MC steps, Figures 20b and c show the state of the simulation. *Note*: this was not a true intermediate state as in MD simulations but rather a snapshot of what the preferred final configuration was trending towards. As can be observed, the preferred mechanism is to have the Ag atoms move from core positions to the shell, while Cu atoms move into the core. As the simulation progressed, fewer Ag atoms were present in the "core" region and progress towards the final state became asymptotically slower. While these simulations have not yet reached an equilibrium structure, it is believed that the lowest energy state has been unambiguously identified as the Cu-Ag core-shell structure. While simulation methods exist that will further push this system towards a true energetic minimum [20], these have not been pursued. The results shown in Figures 19 and 20 show an obvious trend towards a core/shell structure, and this structure has been identified as favorable in both simulations and experiments [20, 14]. With the clear indication that this AgCu EAM potential also favors the correct structure, it is more instructive to calculate properties of this system for use in a phenomenological model than to continue the simulations.

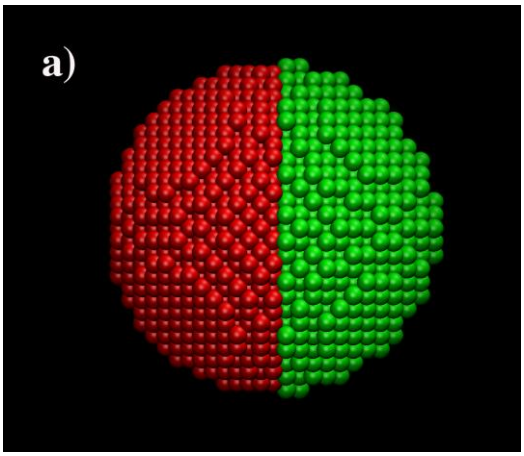

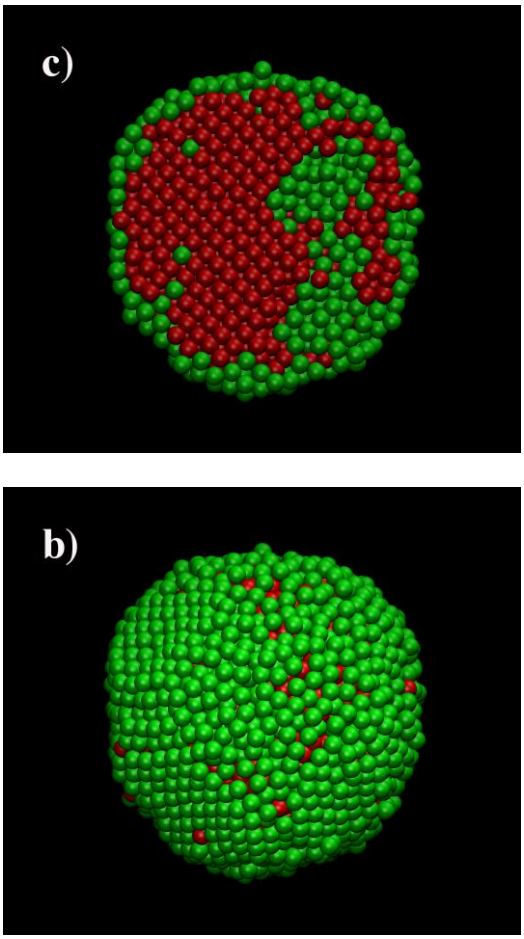

Figure 10. Snapshots from the MC simulation after (a) 0 MC steps (b) 400 million MC steps and (c) 400 million MC steps in cross-section. Colors are the same as in Figure 19.

Since simulation and experimental data indicated a preferential arrangement of Ag along Cu {111} planes [14,17], the interfacial energies of Ag and Cu slabs (periodic in x and y) were calculated with varying crystal orientations. Slabs of Ag{100} (37 X 5.1 X 2.6 nm), Ag{111} (37 X 5.1 X 3.5 nm), Cu{100} (37 X 5.1 X 2.0 nm) and Cu{111} (37 X 5.1 X 3.3 nm) were generated and energy minimized. For the {100} planes, the perpendicular directions are [0 1 0] and [0 0 1], while for the {111} planes, they are [1 1 -2] and [-1 1 0]. There is no mutual rotation of the slabs considered for the interface calculations, and the dimensions perpendicular to the interface (i.e. x and y) were chosen such that they are reasonably close to multiples of the lattice constants of the two metals. This is in an attempt to minimize the contribution of the strain energy to the interfacial energy. Because the calculated energies agree well with previous calculations by other investigators (see below), this procedure appears to be reasonable. The energy of an individual slab will have two components as shown in equation 11.

$$\mathbf{E_{slab} = N*E_{coh} + 2A\gamma_s} \qquad \mathbf{(11)}$$

Where E_{slab} is the total (minimized) energy of the slab, N is the number of atoms, E_{coh} is the cohesive energy, A is the cross-sectional area and γ_s is the surface energy. The cohesive energy is calculated from an energy minimization of a 500 atom cube (with periodic boundary conditions in all three dimensions) of the individual components. Based on these calculations, the cohesive energies were found to be -2.85 eV/atom for Ag and -3.54 eV/atom for Cu, which are in agreement with literature values [18, 20]. The various combinations of the Ag/Cu surfaces were then be put into contact and the interfacial energies calculated using equation 12.

$$\mathbf{E = N(Ag)*E_{coh}(Ag) + A_{slab}\gamma_s(Ag) + N(Cu)*E_{coh}(Cu) + A_{slab}\gamma_s(Cu) + A_{slab}\gamma_{CuAg}} \quad \mathbf{(12)}$$

By calculating N* E_{coh} for each slab separately, and calculating E_{CuAg} from an energy minimization of the interface, the value for γ_{CuAg} was calculated and the results are shown in Table 2. These data indicate that Ag{111}/Cu{111} has the lowest energy of all the interfaces studied, explaining previous results. The calculated interfacial energies were in good agreement with previous interfacial energies that were calculated using a different EAM potential; the energies of semicoherent interfaces were found to be 0.231 J/m^2 for {111} and 0.530 J/m^2 for {100} (10). For comparison, in Table 2 we also show the surface energies of the various orientations of Ag and Cu, as calculated for this EAM potential. Note that these surface energies are significantly higher than the interfacial energies.

Table 2. Interfacial and surface energies of various Ag/Cu slabs calculated through Equations 11 and 12.

γ (J/m^2)	Cu{100}	Cu{111}	Surface γ_{Ag}
Ag{100}	0.5323	0.4331	0.940 [20]
Ag{111}	0.4752	0.1970	0.862 [20]
Surface γ_{Cu}	1.345[9]	1.239[9]	

4.3. Model Development

Based on the results from MD and MC simulations, a model that predicts the energy gained by the formation of a core/shell structure by two distinct nanoparticles is developed. The major assumptions that are made in order to construct this model are that both the initial and final geometries of the nanoparticles are spherical, and that the particles are both pure metals. While these assumptions are unlikely to be accurate depictions of experimentally synthesized nanoparticles (or the core/shell structure they might form), they enable determination of both the initial surface energies as well as the final interfacial energies without the difficulties of understanding the effects of, for example, impurities, solvents/coatings, facets, kinks, or steps. This model, then, is a simplification of the energetics of core/shell formation that only accounts for the effects of surface and interfacial energies.

The energy of a lone, spherical nanoparticle is given by equation 13, similar to Equation. 11, but in this case with only one surface,

$$\mathbf{E_{sphere} = N*E_{coh} + A\gamma_{sphere}} \quad \mathbf{(13)}$$

With A being the surface area of the sphere (see equation 17), and γ_{sphere} being the surface energy of the spherical particle. This surface energy is different from γ_s in equations 11 and 12 because of the variety of exposed faces in the sphere. The energy for two non-interacting nanoparticles is given by equation 14.

$$\mathbf{E_2 = E_{sphere}(Ag) + E_{sphere}(Cu)} \qquad \mathbf{(14)}$$

Similarly, the energy of a core/shell particle would then be given by a combination of the spherical nanoparticle equation as shown in equation 15, where there is no longer a contribution from the surface energy of the Cu, as the entire surface of the Cu core is contacting the inner surface of the Ag shell.

$$\mathbf{E_{c/s} = N(Ag)*E_{coh}(Ag) + A_{Ag}\gamma_{shell}(Ag) + N(Cu)*E_{coh}(Cu) + A_{Cu}}\ \gamma_{\mathbf{sphere}}(\mathrm{AgCu}) \qquad \mathbf{(15)}$$

In equation 15, the surface energy of the Ag in the core/shell structure will be different than that for the bare particle in equation 3, because of the different radius of the two structures (i.e. the same amount of Ag will form a larger sphere when coating a Cu particle). To make this distinction clear, the surface energy in this case is denoted as γ_{shell}. The interfacial energy is now denoted as γ_{sphere}(AgCu), to differentiate the value in a spherical geometry from that used in equation 12. When equation15 is reduced to its analytical components, the relationship shown in equations 16-17 is developed.

$$\mathbf{N = 4/3\pi\, r^3 \rho_m} \qquad \mathbf{(16)}$$

$$\mathbf{A_m = 4\,\pi\, r_m^2} \qquad \mathbf{(17)}$$

Where r_m is the radius of the nanoparticle, ρ_m the number density of the metal *m*, and A_m is the surface area of the nanoparticle. In equation 16 the number of atoms N is written in terms of the density of the element and the volume of the particle, while equation 17 ensures that the surface and interfacial energies in equation 15 are independent of the surface area. The values of γ_{sphere} are determined by calculating the energy of nanoparticles, using equation 13 to eliminate the contribution from the cohesive energy, and fitting the data as a function of nanoparticle radius. Fits for Ag and Cu nanoparticles are shown in Figure 22, with γ_{sphere}(Ag)=1.024 J/m^2 (0.063891 eV/A^2) and γ_{sphere}(Cu) =1.486 J/m^2 (0.092733 eV/A^2). These values, while slightly larger, are close to the calculated slab surface energies shown in Table 2. The comparison is not exact given that the nanoparticles have a variety of exposed surface textures.

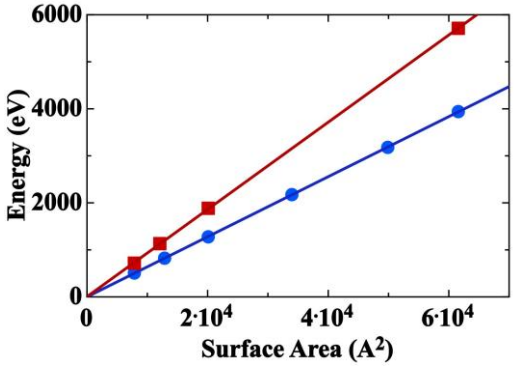

Figure 21. Surface energy contribution of Ag (red squares) and Cu (blue circles) nanoparticles as a function of surface area. Calculated values are shown as squares and fits are shown as solid lines.

The final parameter necessary for Equation 15 is the interfacial energy $\gamma_{\mathbf{sphere}}$(AgCu) between the Cu core and the Ag shell. The energy of a number of core-shell particles with varying size Ag shells (initial Ag nanoparticle radii of 10, 14, 20 and 25 nm) and Cu cores (radii 5, 10, and 14 nm), both cut from single crystal bulk materials, have been calculated in order to arrive at a value for $\gamma_{\mathbf{sphere}}$(AgCu). As with the single nanoparticles shown in Figure 1a, these particles have a variety of exposed surface textures, since the bulk single crystal is oriented with the x,y, and z axes aligned along the [100], [010] and [001] directions, respectively. The calculation of a universal value for γ_{CuAg} is difficult, as smaller radii Cu cores lead to a contribution from curvature, while smaller Ag NPs lead to a dependence on the final shell thickness. While these contributions should be negligible given large enough initial particles, these calculations show that $\gamma_{\mathbf{sphere}}$(AgCu) ranges from about 0.70 - 0.74 J/m^2 (0.044 - 0.046 eV/A^2). These calculated values of $\gamma_{\mathbf{sphere}}$(AgCu) are higher than, but comparable to the largest value shown in Table 2, as discussed above for the values of $\gamma_{\mathbf{sphere}}$(Ag) and $\gamma_{\mathbf{sphere}}$(Cu). For the predictions of the theory, the larger value of $\gamma_{\mathbf{sphere}}$(AgCu) was used as this will only overestimate the interfacial energy, and thus underestimate the energy difference between the core-shell configuration and two separate nanoparticles. Specifically, the energy gained upon core-shell formation was determined by equations 8 and 9.

$$\mathbf{E_{gain} = E_{c/s} - E_2} \qquad \mathbf{(18)}$$

$$\mathbf{E_{gain} = [\gamma_{shell}(Ag)A_{Ag\ shell} - \gamma_{sphere}(Ag)A_{Ag\ NP}] + [\gamma_{sphere}(AgCu)A_{Cu} - \gamma_{sphere}(Cu)A_{Cu\ NP}} \qquad \mathbf{(19)}$$

Where $\boldsymbol{\gamma_{\mathbf{shell}}}$ and $\boldsymbol{\gamma_{\mathbf{sphere}}}$ refer to the surface energies in the shell and original spherical geometry, respectively. Since γ_{sphere}(Cu) is always larger than $\gamma_{\mathbf{sphere}}$(AgCu) the second component of equation. 19 should be negative (see below). This last statement justifies the selection of the largest values of $\gamma_{\mathbf{sphere}}$(AgCu); larger values will lead to an upper bound of E_{gain}.

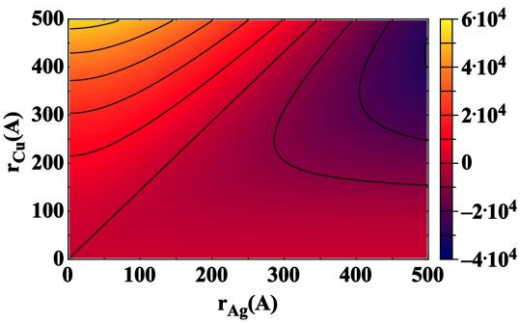

These terms represent all that is necessary to calculate E_{gain} as a function of the radii of the two initial particles. A contour plot of the calculated E_{gain} is shown in Figure 22. The plot shows that the ideal choice for core-shell formation is to utilize relatively small Cu particles as the core with larger Ag particles to act as a shell. For any value of r_{Cu}, the energy gained increases (i.e., becomes more negative) as r_{Ag} increases. However, for certain large r_{Cu} values with small r_{Ag}, there is no energy gained, and the core-shell structure become unfavorable. Note that this plot is less accurate when either r_{cu} is small (due to curvature effects in the surface energies) or r_{Ag} is small (because of incomplete shell formation; see discussion below).

Figure 22. Energy gained (eV) from formation of a core/shell structure plotted as a function of the initial (i.e. unjoined) particle radii.

To better understand the results of Figure 22, it is useful to consider the separate contributions from Equation 19; the first bracketed term representing the difference in the Ag surface energy upon forming a shell from a separate NP, while the second bracketed term is the difference between the Ag/Cu interfacial energy and the surface energy of a bare Cu NP. For a given r_{Ag} the first term increases with increasing r_{Cu}. The reason for this lies in the difference in the outer radius of a core-shell as compared to a bare particle. The radius of a core-shell is $(r_{Ag}^3 + r_{Cu}^3)^{1/3}$, indicating that as r_{Cu} becomes larger (compared to r_{Ag}) the final core-shell radius remains close to that of the initial Cu NP. This is a result of the larger area that must be coated by the same number of Ag atoms, resulting in a thinner shell overall. The larger final radius leads to a larger contribution to the surface energy from the Ag in the core-shell, as opposed to the smaller Ag NP. Note that this contribution to Equation 19 is never negative. In contrast, the second term is always negative, and becomes larger (i.e. more negative) with increasing r_{Cu} because, as discussed above, the interfacial energy is always lower than the Cu NP surface energy. There is no dependence on r_{Ag} in this term, as would be expected from this simple model, but this is exactly where the inaccuracies of the model in Figure 22 arise. With smaller initial r_{Ag}, it is impossible for the Ag to fully coat the Cu, resulting in incorrect estimates of three terms in Equation 19. Specifically the contribution Cu surface energy of the core-shell structure is underestimated (in fact, it is completely ignored), while the Ag surface energy and the AgCu interfacial energy are both overestimated. It is therefore expected that the values shown in Figure 22 are an upper bound of the energy gain. The shell thickness is given by

$$\mathbf{r_{shell} = (r_{Ag}^3 + r_{Cu}^3)^{1/3} - r_{cu}} \qquad (20)$$

which indicates that for most cases with rAg < rCu the shell will be incomplete (i.e. the thickness is less than the size of a Ag atom), and thus Figure 22 can only be used as a guide for optimal initial conditions. As an example, it is clear from our experiments [14] that Ag and Cu NPs with initial radii of 6 and 12-15nm will form core-shell structures, although Figure 22 would imply that this is not energetically favorable. Clearly, the difference in surface energy results in the Ag wetting the Cu, regardless of the initial size of the particles.

It is possible to modify Equation 19 to include a correction factor for incomplete coverage. The fractional coverage, f, can be estimated by

$$\mathbf{f = r_{shell} / \sqrt{2}\alpha_{Ag}} \quad (21)$$

where α_{Ag} is the lattice constant of Ag, and the $\sqrt{2}$ estimates the spacing between neighboring {111} layers. This factor modifies Equation 19 to be

$$\mathbf{E_{gain} = f\gamma_{shell}(Ag)A_{Ag\ shell} - \gamma_{sphere}(Ag)A_{Ag\ NP} + (1\text{-}f)\gamma_{sphere}(Cu)A_C + f\gamma_{sphere}(AgCu)A_{Cu} - \gamma_{sphere}(Cu)A_{Cu}} \quad \mathbf{(22)}$$

in the cases where $f \leq 1.0$ only; when $f = 1.0$ Equation 12 reduces to Equation 19. A contour plot of the modified energy is shown in Figure 23, in which many of the erroneous effects of fractional coverage (specifically when $r_{Ag}<r_{Cu}$) are removed, indicating an energetic gain for most combinations of radii.

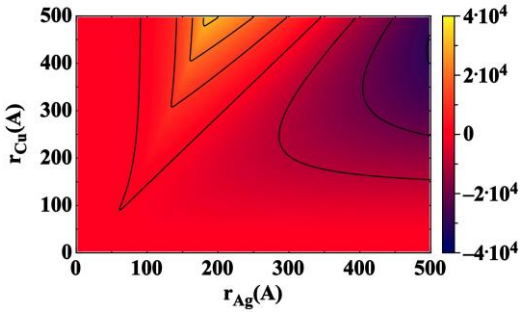

Figure 23. Energy gained (eV) from formation of a core/shell structure including estimates of the effects of fractional shell coverage.

4.4. Conclusions

While the formation of a core-shell structure has been previously understood from the standpoint of competing surface energies and atomic sizes, the model developed here is the first demonstration of the energetics of formation, particularly with the radii of the initial particles taken into account. This model indicates that for the Cu-Ag core-shell arrangement, relatively smaller particles of Cu and larger particles of Ag are the most energetically favorable to form a core-shell structure. In addition, this structure was calculated to be the most favorable to form along {111} faces, which has also been seen experimentally. This is an extension of the experimental work that demonstrated the formation of a core-shell structure from initially distinct particles, rather than through a co-deposition process [14]. It is expected that this model can prove useful, both for directing synthesis routes for nanoparticles, as well as for choosing specific metallic species which are more or less likely to form such core-shell structures, depending on the desired use.

5. References

1. Y. Morisada *et al.*, J Elec. Mater. 39, 1283 (2010)
2. Rodriguez, M. A.; Boyle, T. J.; Yang, P.; Harris, D. L., *Powder Diffraction* **2008,** *23*, 121.
3. Bunge, S. D.; Boyle, T. J.; Headley, T. J., *Nano Letters* **2003** *3* 901-905.
4. Hiramatsu, H.; Osterloh, F. E., *Chem. Mater.* **2004,** *16*, 2509-2511.
5. Gerung, H.; Boyle, T. J.; Tribby, L. J.; Bunge, S. D.; Brinker, C. J.; Han, S. M., *J. Am. Chem. Soc.* **2006,** *128*, 5244-5250.
6. Gerung, H.; Bunge, S. D.; Boyle, T. J.; Brinker, C. J.; Han, S. M., *Chem. Commun.* **2005,** *14*, 1914-1916.
7. Zeng, G.; McDonald, S.; Nogita, K. *Microelectronic Reliability **2012***, 52, 1306-1322.
8. Morita, T.; Ide, E.; Yasuda, Y.; Hirose, A.; Kobayashi, K. Japanese J. Appl. Phys. **2008**, 47, 6615-6622.
9. Morisada, Y.; Nagaoka, T.; Fukusumi, M.; Kashiwagi, Y.; Yamamoto, M.; Nakamoto, M., Kakiuchi, H.; Yoshida, Y. *J. Elec. Mater* **2011**, 40, 2398-2402.
10. Morisada, Y.; Nagaoka, T.; Fukusumi, M.; Kashiwagi, Y.; Yamamoto, M.; Nakamoto, M. *J. Elec. Mater* **2010**, 39, 1283-1287.
11. Allard, L. F; Flytzani-Stephanopoulos, M.; Overbury, S. H. *Microsc. Microanal***. 2010,** 16, 375-385.
12. Pennycook, S.J.; Jesson, D.E. *Phys. Rev. Lett*. **1990,** 64, 938-941.
13. Sutter, E.; Sutter, P.; Zhu, Y.M. *Nano Letters* **2005**, 5, 2092-2096
14. Lu, P.; Chandross, M.; Boyle, T.J.; Clark, B.; Vianco, P. Equilibrium Cu-Ag Nanoalloy Structure Formation Revealed by *in situ* Scanning Transmission Electron Microscopy Heating Experiments. *APL Mat.* **2014**, *2*, 022107.
15. Williams, P.L.; Mishin, Y.; Hamilton, J.C. An Embedded-Atom Potential for the Cu–Ag System. *Modelling Simul. Mater. Sci. Eng.* **2006**, *14*, 817-833.
16. Foiles, S.M. Private communication, **2012**.
17. Baletto, F.; Mottet, C.; Ferrando, R. Growth Simulations of Silver Shells on Copper and Palladium Nanoclusters. *Phys. Rev. B* **2002**, *66*, 155420.
18. Mishin, Y.; Mehl, M.J.; Papaconstantopoulos, D.A.; Voter, A.F.; Kress, J.D. Structural Stability and Lattice Defects in Copper: Ab Initio, Tight-Binding, and Embedded-Atom Calculations. *Phys. Rev. B* **2001**, *63*, 224106.
19. Dregia, S.A.; Wynblatt, P.; Bauer, C.L. Computer Simulations of Epitaxial Interfaces. *Mat. Res. Soc. Symp. Proc*. **1989**, *141*, 399-404.
20. Ferrando, R.; Jellinek, J.; Johnston, R.L. Nanoalloys: From Theory to Applications of Alloy Clusters and Nanoparticles. *Chem. Rev.* **2008**, *108*, 845-910.

6. List of journal publications and conference presentations/proceedings supported

6.1. Journal publications

1. "Equilibrium Cu-Ag nanoalloy structure formation revealed by in-situ scanning transmission electron microscopy heating experiments"
   P. Lu, M. Chandross, T.J. Boyle, B.G. Clark and P. Vianco, *APL Materials 2*, 22107 (2014)
2. "Atomic-scale chemical imaging and quantification of metallic alloy structures by energy-dispersive X-ray spectroscopy"
   P. Lu, *et al*. *Sci. Rep. 4*, 3945 (2014)
3. "Chemical Quantification of Atomic-scale EDS Maps under Thin Specimen Conditions"
   P. Lu, E. Romero, S. Lee, J. L. MacManus-Driscoll, and Q. Jia, *Microscopy and Microanalysis* -accepted for publication (Sept-2014)
4. "Atomic-scale chemical quantification of oxide interfaces using energy-dispersive X-ray spectroscopy"
   P. Lu, J. Xiong, M. Van Benthem and Q. Jia, *Applied. Physics Letter 102*, 173111 (2013)
5. "Energetics of the Formation of Cu-Ag Core-Shell Nanoparticles", M. Chandross, *"Modeling and Simulation in Materials Science and Engineering*, accepted for publication.
6. "Diffuse Interface Model for Solid State Wetting in Nanoscale Alloys," F. Abdeljawad and M. Chandross, in preparation
7. "In-situ STEM observation of Au NPs and Ge Rods interaction at elevated temperatures"
   P. Lu *et al,* in preparation.

6.2. Conference presentations/proceedings

1. "*In-situ* TEM Study of Cu and Ag Nanoparticle Interaction"
   P. Lu, T. Boyle, B. Clark and M. Chandross, Microscopy and Microanalysis, August, 2013
2. In-situ TEM study of Cu-Ag nanoparticle thermal interaction"
   P. Lu et al, in the 25th Rio Grande Symposium on Advanced Materials, Oct. 7. 2013
3. "Bonding of Metallic Nanoparticles"
   M. Chandross, T. Boyle, B. Clark, P. Lu, May, 2013. International Conference on Metallurgical Coatings and Thin Films, San Diego, CA 4/29/2013-5/3/2013
4. "Bonding of Metallic Nanoparticles"
   M. Chandross, TMS 2014: Annual Meeting & Exhibition, San Diego, CA, 2/16/2014-2/20/2014
5. "Bonding of Metallic Nanoparticles"
   M. Chandross, The Second International Conference on Metallic Materials and Processing, Las Vegas, NV, 9/29/2014-10/2/2014 (Keynote)
6. "Microstructural Evolution of Binary Nanoparticle Systems",
   M. Chandross, TMS 2015: Annual Meeting & Exhibition, Orlando, FL, 3/15/2015-3/19/2015 (invited)

7. “Morphological Evolution in Metallic Nanoparticles and the Formation of Core-Shell Structures: A Phase-Field Treatment”
   M. Chandross, TMS 2015: Annual Meeting & Exhibition, Orlando, FL, 3/15/2015-3/19/2015
8. “Chemical Quantification of Atomic-scale EDS Maps under Thin Specimen Conditions”
   P. Lu, J. Xiong, M. Van Benthem, and Q. Jia, Microscopy and Microanalysis, August, 2013


Sandia National Laboratories